IEEE Access
Multidisciplinary ⋮ Rapid Review ⋮ Open Access Journal

Received 12 June 2023, accepted 28 June 2023, date of publication 4 July 2023, date of current version 11 July 2023.

Digital Object Identifier 10.1109/ACCESS.2023.3292244

RESEARCH ARTICLE

Comparative Study of Induction and Wound Rotor Synchronous Motors for the Traction Drive of a Mining Dump Truck Operating in Wide Constant Power Speed Range

VLADIMIR DMITRIEVSKII[1], VLADIMIR PRAKHT[1], EDUARD VALEEV[1], ALEKSEY PARAMONOV[1], VADIM KAZAKBAEV[1], AND ALECKSEY ANUCHIN[2], (Senior Member, IEEE)

[1]Department of Electrical Engineering and Electric Technology Systems, Ural Federal University, 620002 Yekaterinburg, Russia
[2]Department of Electric Drives, Moscow Power Engineering Institute, 111250 Moscow, Russia

Corresponding author: Alecksey Anuchin (anuchinas@mpei.ru)

This work was supported by the Ministry of Science and Higher Education of the Russian Federation under Project FSWF-2023-0017.

ABSTRACT Motors with rare earth permanent magnets are the most compact and energy efficient in most applications. However, their use as traction motors for off-highway vehicles, such as mining dump trucks, is challenging not only because of the high cost of the magnets, but also because of the difficulty of providing a wide range of constant power speed control due to the unregulated permanent magnet flux. For this reason, induction motors remain the most popular type of motor for hybrid and all-electric mining dump trucks. However, the use of an induction motor results in increased power loss, increased current, and high temperature ripple of the power switches of the solid-state inverter when stopping on a slope with an electric brake. In this article, a theoretical comparison between an induction motor (IM) and a magnet-free wound rotor synchronous motor (WRSM) with a rotor DC-excitation in a mining dump truck drive is presented. Both motors have an identical stator outer diameter, and their geometry is optimized using the Nelder-Mead method. 2D finite element analysis in the time domain is used to calculate the IM characteristics. Steady-state characteristics of the motors such as efficiency, losses, torque ripple, required inverter power, dimensions, weight and cost of active materials are compared. In addition, losses and temperature ripples in the power modules of the semiconductor inverter, which affect the reliability of the drive, are compared when using the considered motors. The study demonstrates that the WRSM offers significant benefits such as reduced power loss, inverter power requirement, cost and mass of active materials, making it promising for use in mining trucks.

INDEX TERMS AC machines, automotive applications, brushless motors, electric vehicles, electromagnetic modeling, mining industry, traction motor.

I. INTRODUCTION

Nowadays, most traction drives of the subway, railway locomotives, trolleybuses, trams, electric and hybrid buses, tractors, as well as mining dump trucks use induction (asynchronous) motors (IMs) [1], [2], [3], [4]. For example, IMs are used in the drives of passenger electric vehicles Audi e-tron S [5] and Tesla model S [6]. Induction motors do not contain expensive rare earth magnets and are cheaper than permanent magnet synchronous motors (PMSMs). However, traction drives with induction motor have the following disadvantages:

1) Large losses and heating in the rotor [7], [8] can lead to unacceptably high temperature of the rotor core, shaft and bearings, even if using the liquid cooling of the rotor [9];

2) The weight and size are significantly larger than those of permanent magnet synchronous motors (PMSM);

The associate editor coordinating the review of this manuscript and approving it for publication was Paolo Giangrande.

3) If a constant power speed range (CPSR) more than 3 is required then a large power rating of the solid-state traction invertor is necessary [4], [10]. For example, in [4], it is shown that a traction drive based on an IM with a mechanical power of 50 kW and a CPSR of 3.5 uses an inverter with a power rating of 125 kVA. In [10], it is shown that an IM-based traction drive with a mechanical power of 50 kW and with a CPSR of 4 also uses an inverter with a power rating of 125 kVA;

4) Sometimes it is necessary to stop mining dump trucks (for example, to let another vehicle pass) [11], cars (for example, while waiting at a traffic light) [12], trolleybuses, electric buses, trams and other electric vehicles on a slope using the electric traction motor at zero rotor speed as a brake, without using the mechanical parking brake. In this case, due to the need for a slip between the stator and rotor frequencies in an IM, the stator frequency is not zero, and the motor is powered by a low frequency current with a large amplitude. As a result, large-amplitude low-frequency temperature fluctuations occur in the power switches of the inverter, which eventually lead to the destruction of the switches, that is, to a much faster depletion of the service life [13]. Therefore, in order to make the inverter service life acceptable when using an IM, it is necessary to significantly increase the inverter power rating [14]. At the same time, synchronous motors can stop a vehicle on a slope with zero rotor speed and constant currents in the stator phases. When stopping on a slope, the losses in the inverter switches of a synchronous drive are almost constant over time, and there is no large temperature ripple. Audi e-tron S model and old Tesla's model (Tesla model S) use induction motor [5], [6]. In these vehicles, a short stop on a slope (for example, at a traffic light) is performed using a mechanical brake, which, according to users of the electric vehicles, is less convenient than a short stop using an electric motor [15]. Moreover, in new Tesla's models (for example, Tesla model 3) and Audi (for example, Audi Q4 e-tron), induction motors have been replaced by synchronous motors with rare earth magnets [16], [17].

A. ADVANTAGES OF SYNCHRONOUS MOTORS WITH ELECTRIC EXCITATION WITHOUT RARE EARTH MAGNETS

Synchronous motors with rare-earth is a widely used alternative to traction IMs. Such PMSMs provide a large specific torque and the ability to create a braking torque at a standstill at a constant current in phases [18]. However, the widespread use of PMSM in subway drives, railway trains, mining equipment, tractors and trucks is hampered by the following reasons:

1) High cost due to the use of expensive rare earth magnets;

2) A large value of uncontrolled armature electromotive force (EMF) at a non-zero speed, which may cause a fire hazard in the event of an emergency short circuit;

3) Permanent magnets used in traction motors may undergo irreversible demagnetization due to the high operating temperatures (above 120 °C), which can lead to a significant deterioration in their properties;

4) The use of rare-earth magnets creates a technological dependency on a limited number of suppliers of rare-earth elements [19]. Prices of these elements are unstable and may fluctuate several times over a few years [20], [21];

5) The extraction of rare earth elements necessary for the production of rare earth magnets causes great harm to the environment [22];

6) In applications that require a wide (CPSR), large losses and heating at high speeds occur, caused by the need to compensate for the uncontrolled magnetomotive force (MMF) of permanent magnets with the opposite component of the stator current when implementing the field weakening strategy [23]. For example, the article [23] shows the inexpediency of using a PMSM in the drive of a mining dump truck with a CSPR of 10:1 and the relatively better performance of a synchronous homopolar motor with an excitation winding on the stator.

Therefore, the problem of developing new traction motors without rare earth magnets, which at the same time do not have large losses in the rotor and operational problems associated with slip, is relevant. To this end, leading electric vehicle manufacturers, including BMW [24], [25] and Renault [26], [27], [28], have developed magnet-free synchronous motors, also known as wound rotor synchronous motors (WRSMs), for their electric vehicle models such as BMW iX3, Renault Zoe, Renault Fluence, and Renault Megane E-TECH. These motors have a DC excitation winding on the rotor that allows for the control of the excitation flux and reduces the power rating required for the traction inverter [29], [30]. These developments in electric vehicle motor technology provide a promising direction towards magnet-free and more efficient electric vehicles. However, these motors have a disadvantage, as they use sliding contact (slip rings) to supply current to the excitation winding on the rotor, which may reduce reliability and complicate vehicle maintenance. This challenge can be solved by using a brushless exciter, which eliminates the need for sliding contacts.

This problem of WRSMs can be solved by using a brushless exciter [31], [32]. This challenge can be solved by using a brushless exciter, which eliminates the need for sliding contacts [31], [32]. Most traction WRSMs with brushless exciters were initially designed as generators [31] but have recently been introduced as traction motors [30], [32], [33]. These motors use a rotating transformer as a brushless exciter, with the primary winding located on the stator and the secondary winding and diode rectifier on the rotor [30]. High-frequency brushless exciters are commonly placed in the space under the end parts of the stator winding, allowing for a compact design without increasing the length of the motor [30], [32], [34]. Some companies have already announced the release of compact high-frequency brushless exciter traction WRSMs [35], [36].

B. OVERVIEW OF LITERATURE ON THE DESIGN OF INDUCTION MOTORS FOR APPLICATIONS WITH A WIDE CPSR

The article compares the performance of induction motors (IM) and wound rotor synchronous motors (WRSM) in a hybrid mining dump truck drive. Specifically, the study compares the motors' performance and cost for a wide speed range of 400 to 4000 rpm at a constant mechanical power output of 370 kW (CPSR 10:1). The authors demonstrate that the WRSM has better performance and specific characteristics than IM, with significant advantages in terms of cost and mass of active materials. The cost of active materials of the motors and the cost of inverter power modules for WRSM and IM are compared as well. Moreover, the use of the WRSM is shown to improve the reliability and prolong the service life of a traction semiconductor inverter by reducing the temperature ripple of the power switches in the electric brake mode, a common operation mode used for mining dump trucks [37]. This study builds on previous research that compared the performance of SHM, PMSM, and WRSM in a hybrid mining dump truck drive [23], [38], where it was found that the PMSM may have complications due to large losses and heating at high rotational speeds. Overall, the results suggest that the WRSM is a promising option for hybrid mining dump truck drives with a wide speed range.

Many articles were devoted to the optimization of IMs and comparison of IMs with other types of motors for electric vehicles. For example, article [39] compares performances of traction IPMSM (interior permanent magnet synchronous motor), SPMSM (surface permanent magnet synchronous motor) and IM in an application with a CPSR of 3:1. Computer-aided optimization of the characteristics of the motors before their comparison was not carried out. The advantage of the IPMSM and the IM over the SPMSM in a broader CPSR is shown, however, it is noted that IM has higher losses than the IPMSM. Article [40] compares the performance of high speed IPMSM, SRM (switched reluctance motor) and IM in a traction application with a CPSR of 5:1. Computer aided optimization of the characteristics of the motor in this study was not carried out. The advantages of the IPMSM in small dimensions and the advantages of the SRM in high rotor strength are shown. The advantages of the IM are the absence of the risk of irreversible demagnetization of the magnets, losses in the magnets and large ventilation losses. At the same time, the disadvantage of the IM is that the total power loss is significantly greater than that of the IPMSM.

C. THE PROBLEM AND AIM OF THE STUDY

This article compares the characteristics of the WRSM and IM in a traction application with a wide CPSR of 10:1, including torque ripple, efficiency, and the required power rating of the solid-state inverter, providing a novel theoretical comparative study to the topic. This article also analyzes and compares temperature ripple in the traction inverters when using the considered motors, which was not previously presented in the literature when comparing traction drives based on WRSM and IM. Theoretical characteristics of the WRSM, obtained in a previous study, are compared with the calculated characteristics of the IM [38]. The design optimization of both considered motors was carried out using the same approach based on the two-dimensional finite element analysis (FEA) and the Nelder-Mead method.

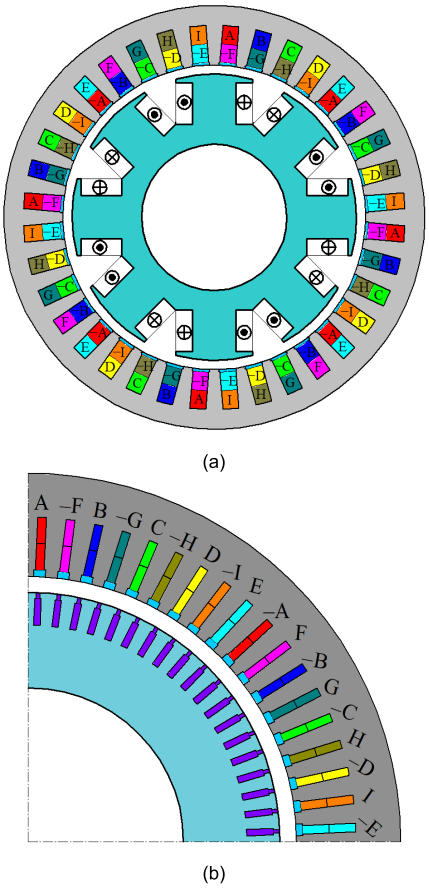

FIGURE 1. Comparison of design features: (a) wound rotor synchronous motor (WRSM) with a DC excitation winding (b) induction motor (IM).

II. THE DESIGN CHARACTERISTICS OF THE MOTORS UNDER CONSIDERATION

The two machines under consideration feature an 8-pole, 9-phase winding. The WRSM uses a double-layer armature winding, and there are layers of different phases in the stator slots. In the IM, the armature phase zone layout is single-layer, as shown in Fig. 1, although for convenience of laying operation, the turns of the coil in one slot are divided into two insulated layers, as shown in Fig. 2b, and the number of turns per slot must be even. In Fig. 1, capital letters A to I indicate the motor phases. The negative sign next to the current in Fig. 1 indicates that the current in the winding layer is flowing in the opposite direction compared to the other winding layers. The WRSM stator has 36 teeth, while IM stator has 72 teeth. The stator slots number per pole and per phase q is $36/(8{\cdot}9) = 0.5$ and $72/(8{\cdot}9) = 1$, respectively. The WRSM winding has two rectangular strands per turn. A turn of the IM has a single strand as shown in Fig. 2.

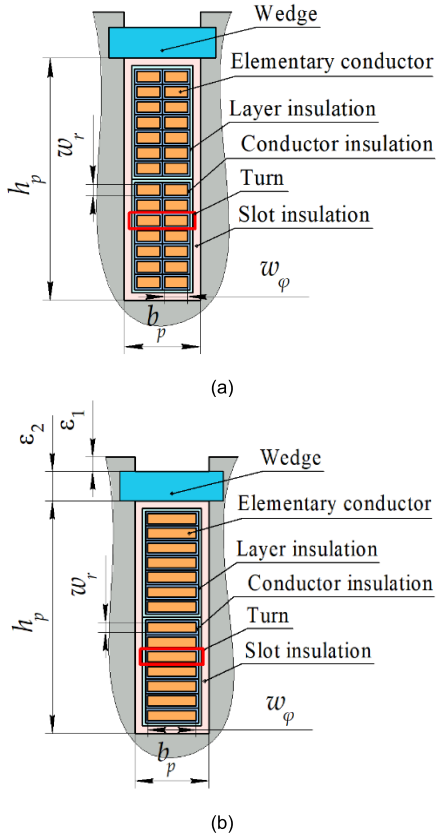

FIGURE 2. Open-type stator slot layout: (a) WRSM (b) IM.

The IM rotor has 76 teeth. A squirrel cage rods of rectangular shape are located in the teeth. The rods are short circuited by end rings. The end rings have openings for the rods' end. After welding to the rods, these openings are filled, and the plates can be considered as solid disks. It is assumed that the magnetic cores of both the rotor and the stator of the IM are made of the same M270-35A steel with a thickness of 0.35 mm.

The electric motors are connected to a nine-phase inverter, which is formed by three individual three-phase modules, with each module supplying power to three motor phases (Fig. 3). The maximum line-to-line voltage of 1000 V is limited by the voltage in the DC link. Discontinuous space-vector modulation is used for each of the three-phase modules [41]. Compared to a three-phase inverter, the nine-phase inverter enables a reduction in the current rating of individual power modules and improves reliability in case of individual power module failure. The nine-phase winding in the motor increases the winding factor and improves the spectral composition of the magnetomotive force.

The WRSM has been optimized in a previous study [38], and the IM optimization results are presented in this article. Both motors must meet the traction characteristic requirements of the BELAZ 75570 mining dump truck drive, which requires a constant mechanical output power of 370 kW in the speed range from 400 rpm to 4000 rpm (10:1, Fig. 4). The

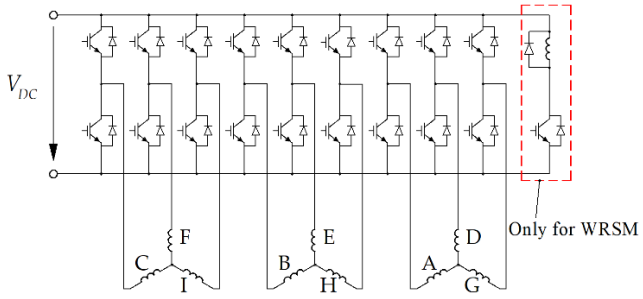

FIGURE 3. Scheme of the inverter for the nine-phase traction motor. Capital letters A to I indicate the motor phases.

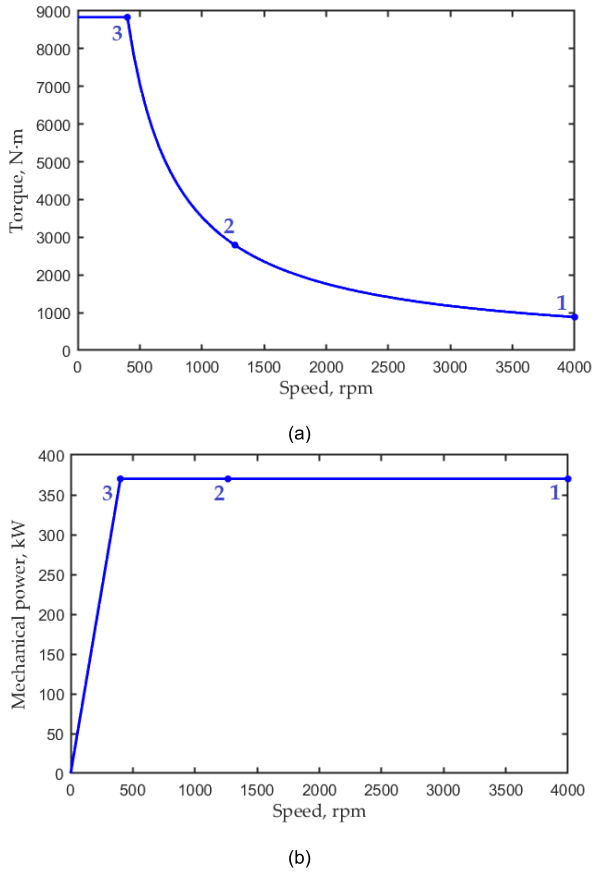

FIGURE 4. Traction characteristics of the considered traction electric drive: (a) Torque versus speed curve; (b) Output mechanical power versus speed curve. Numbers 1,2 and 3 designate the numbers of operating points described in Table 1.

optimization parameters, objectives, and results are described in detail, and only the final results of the IM optimization are presented in this study.

III. BRIEF DESCRIPTION OF THE MATHEMATICAL MODEL OF THE INDUCTION MOTOR

This study aims to investigate the steady-state characteristics of both WRSM and IM for given sinusoidal phase currents. In a WRSM, the current distribution is known in advance, and a stationary simulation is carried out based on a set of magnetostatic problems corresponding to different rotor positions.

In the case of an IM, it is necessary to calculate the current density distribution in the rotor bars. There are many approaches to steady-state simulation of an IM [42]. However, only time-domain simulation accurately takes into account such phenomena as cores saturation depending on the time, minor harmonics, etc.

The time-domain two-dimensional FEA of the IM is usually carried out under the assumption of a plane-parallel magnetic field, which can be described by a vector magnetic potential having only the normal component A_z. The components of magnetic flux density have the form:

$$B_x = \frac{\partial A_z}{\partial y};\ B_y = -\frac{\partial A_z}{\partial x}. \tag{1}$$

Considering the constitutive equations expressing the magnetic field strength H through the flux density B, the values of B, H and A_z are determined by the current density normal to the cross section through Ampère's law:

$$\frac{\partial H_y}{\partial x} - \frac{\partial H_x}{\partial y} = J_z. \tag{2}$$

The current density in the phase windings and their flux linkage are defined as:

$$J_z = \sum_i I_i \Xi_i; \tag{3}$$

$$I_i = I_{amp} \cos(\phi - \frac{2\pi i}{9}),\ i = 0, 1, 2, 3, 4, 5, 6, 7, 8; \tag{4}$$

$$\Phi_i = L \iint A_z \Xi_i dS, \tag{5}$$

where L is the length of the stator lamination; Ξ_i is the current density, if a current of 1 A flows through i-th phase, and there is no current in other phases, I_i are the phase currents, I_{amp} is the current amplitude, ϕ is the electric current angle. When the winding current frequency ω is constant, $\phi = \omega \cdot t$, in more general case ϕ is obtained by integrating ω.

The instantaneous phase voltage is determined through the instantaneous flux linkage as:

$$U_i = \frac{d\Phi_i}{dt} + RI_i, \tag{6}$$

where R is the phase resistance.

In windings with solid rectangular conductors with a small number of turns per coil, not only ohmic losses occur, but also significant eddy current losses [43]. The formula to compute the density of the eddy current loss in the winding is:

$$p_{eddy} = \frac{\sigma_{Cu} k_z}{12} \left[w_\varphi^2 \left(\frac{\partial B_r}{\partial t} \right)^2 + w_r^2 \left(\frac{\partial B_\varphi}{\partial t} \right)^2 \right], \tag{7}$$

where σ_{Cu} is the electrical conductivity of copper; w_φ and w_r are the wire section's width and height; k_z is the slot filling factor; B_r and B_φ are the flux density's radial and tangential components, respectively.

The current density in the i-th rod of the rotor squirrel cage is given by the formula:

$$J_z = -\sigma_{squirrel} \left(\frac{dA_z}{dt} + \frac{\phi_i}{L} \right), \tag{8}$$

where d/dt is the substantial time derivative; φ_i is the potential difference at the ends of the rod.

The equation for potential differences has the following form:

$$2\phi_i - \phi_{i-1} - \phi_{i+1} = 2r_{rot} I_i^{squirrel} = 2r_{rot} \int\limits_{i-th\ rod} J_z dS, \tag{9}$$

where r_{rot} is the resistance of a section of the squirrel cage over one rotor tooth pitch; $I_i^{squirrel}$ is the current flowing through the i-th rotor rod; the factor 2 on the right side of the equation takes into account the fact that the rotor rod is limited by two end rings.

The length of the arc in one section with a length of one rotor pole pitch is $2\pi r/N_{rot}$, where N_{rot} is the number of rotor rods, r is the distance to the rotation axis. We also assume that the potential φ on the cross sections of the rings limiting one rotor tooth pitch is constant and the current density is inversely proportional to the length of the arc. Given the above, the squirrel cage resistance per one rotor pitch can be calculated as $r_{rot} = 2\pi\ /(N_{rot} \cdot h \cdot \sigma_{\text{squirrel}} \cdot \ln[R_{ring1}/R_{ring2}])$, where h is the ring thickness, σ_{squirrel} is the conductivity of the squirrel cage material, R_{ring1} and R_{ring2} are external and internal ring radii.

The use of the time-domain 2D model for the IM analysis requires large computational costs due to a long transient process [42], which greatly complicates its application in optimization procedures. In this study, the transient process is accelerated by:

1) Decreasing the specific conductivity of the squirrel cage material by some factor m;

2) Increasing the frequency of the fundamental harmonic of the current in the rotor squirrel cage by the same factor m;

3) The rotor mechanical frequency Ω is assumed to be constant and unchanged.

The angular frequency of the fundamental current in the squirrel cage ω_{r0} can be expressed through the number of pole pairs p, the mechanical rotor angular frequency Ω, and the rotor slip s as follows:

$$\omega_{r0} = \frac{\omega_{r0}}{s} - p \cdot \Omega = \frac{p \cdot \Omega \cdot s}{1 - s}. \tag{10}$$

The stator winding current frequency is equal to $\omega = p \cdot \Omega + \omega_{r0}$. However, if a new value of the angular frequency in the squirrel cage $\omega_r = m \cdot \omega_{r0}$ is increased by m times then $\omega = p \cdot \Omega + \omega_r = p \cdot \Omega + m \cdot \omega_{r0} = p \cdot \Omega + p \cdot \Omega \cdot s \cdot m/(1\text{-}s)$. During the transient process m starts from the value m_0, and then decreases to unity, that is the model equations obtain their natural form. Therefore, the accelerated transient

process is described by the following equations:

$$\begin{aligned}
\sigma_{\text{squirrel}} &= \frac{\sigma_{\text{squirrel0}}}{m};\\
\omega &= p\Omega\left(1+\frac{sm}{1-s}\right);\\
\mathrm{f} &= \int_0^t \omega dt;\\
m &= 1+m_0(1-t/t_0)^{\gamma},\ t<t_0;\\
m &= 1,\ t\geq t_0,
\end{aligned} \tag{11}$$

where $\sigma_{\text{squirrel0}}$ and σ_{squirrel} are the actual electrical conductivity of the squirrel cage material and the electrical conductivity taken during the calculation; m_0 and γ are the parameters that determine the dependence of $m(t)$; t_0 is the time of the transient process with the modified equations.

The system of equations (1), (2), (3), (4), (8) must be solved, while expressions (6) and (7) can be used in post-processing to determine the motor performance. Only (8) in the equation system contains the (substantial) time derivative. The described modification of the equations, that is simultaneous change in the frequency in the squirrel cage and in its specific conductivity, guarantees that current and field distribution of the main harmonic in the IM is unchanged. In particular, the model correctly describes the torque produced by the main harmonic, that is main component of torque. When m becomes nearer to 1, the accuracy of other harmonics increases.

The described approach provides the benefit in the calculation time together with the temporal discretization of the model by the second-order backward differentiation formula (BDF) with a constant step, which provides stable solution for rigid problems. Therefore, large values of m and large changes in ϕ at one step are allowed at the beginning of the calculation without losing stability, although the accuracy of the calculations is not guaranteed. As t increases, m decreases and the accuracy of BDF approximation of the derivatives increases.

The practical use of a mathematical model often involves the calculation of specific points with a given speed, torque and power. In this study, slip is considered an additional input to the calculation, and the current is selected so that at a given speed the required power is obtained. For this, another differential equation is jointly solved:

$$\frac{dI}{dt} = \alpha\left(P_{2\,0} - P_2\right), \tag{12}$$

where P_{20} and P_2 are the set and instantaneous values of the mechanical power; α is the constant that determines the rate of termination of the rotor current transient; I is the current amplitude.

IV. OPTIMIZATION OF INDUCTION MOTOR: PARAMETERS AND OBJECTIVES

The operation points at which the performance of the WRSM and the IM are compared are shown in Table 1. Operating point 1 at a speed of 4000 rpm is identified by the highest electrical frequency of the fundamental current component, maximum losses in steel and additional losses in the winding. It also has the minimum torque. Operating point 3 at a speed of 400 rpm is characterized by the highest copper loss and armature current but has the lowest fundamental electrical frequency. The evaluation of motor performance is typically carried out at these two points since they provide a rough estimate of motor behavior throughout the entire speed range in the field-weakening region. These points are situated at the extreme limits of the speed range, which is why it is important to analyze and optimize the performance of the motor at these points [44].

TABLE 1. Operating points of the traction motors.

Operating point number	Torque, N·m	Rotational speed, rpm	Mechanical power, kW
1	883	4000	370
2	2793	1265	370
3	8833	400	370

This approach is assumed at the optimization because the transient 2D mathematical model is very resource consumptive. The performance of the IM in point 2 is calculated afterwards. The objectives of the IM optimization are average losses over points 1 and 3: $< Plosses >\ = (Plosses1 + Plosses3)/2$, maximum current I_3 (reached in point 3), and mass of the copper M as the most expensive material. The DC voltage (amplitude of line voltage) U_1 (reached in operation point 1) must not exceed the level of 950 V taken with a margin of 50 V. The optimization in this research employs the Nelder-Mead method with a single-criterion, which uses the following form for the objective function:

$$\begin{aligned}
F &= \ln(< P_{losses} >) + \ln(I_3) + 0.1\ln(M)\\
&\quad + \ldots\ldots + 4\begin{cases}\ln(U_1/950), & when\ U_1 > 950\ V;\\ 0, & otherwise.\end{cases}
\end{aligned} \tag{13}$$

The first and second terms in (13) demonstrate that reduction of average losses and maximum current are assumed to be equally valuable. Due to the third term, the IM with less copper mass is preferable. The fourth term creates "a soft wall" to fulfill the voltage constraint.

The simplex Nelder-Mead method can significantly reduce the optimization time compared to methods using populations (genetic algorithm, particle swarm algorithm, etc.), which is important when optimizing the motor performance in several operating points. However, at the same time, the Nelder-Mead method is a single-criteria unconstrained method, which requires a special approach to constructing the objective function when performing multi-criteria constrained optimization [45].

The main objectives of optimization are to reduce the losses and current of the IM, therefore the corresponding terms of the optimization function have a unit weight. Reducing the mass of copper M is not considered as the main goal of optimization, however, an excessive increase in the mass

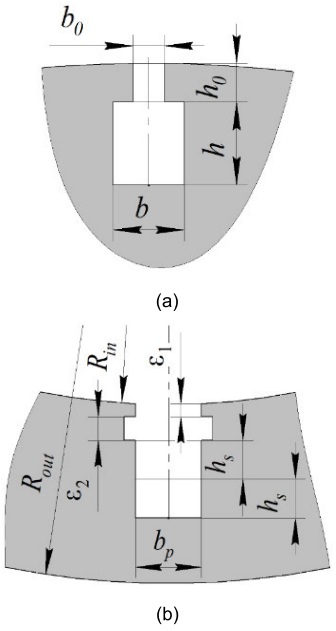

FIGURE 5. Geometric specifications of the induction motor: (a) Rotor details; (b) Stator details.

of copper must be limited. The term ln(M) with a weighting factor of 0.1 is introduced not to reduce the mass of copper due to a smaller reduction in losses and current, but to give preference to a design with a lower mass of copper at approximately the same values of losses and current. In addition, the introduction of even a small weighting factor of ln(M) makes it possible to limit the cross section of the end rings of the squirrel cage of the rotor, which otherwise could grow indefinitely.

Tables 2 and 3 present the fixed and varied parameters during the optimization process. Fig. 5 shows details of the geometry of the stator and rotor. Width and thickness of rectangular winding necessary for calculating losses in it are determined as it did in [38]. To decrease the number of variable parameters, the rotor yoke thickness is assumed to be equal to the stator yoke thickness, and the inner radii of the rotor laminated stack and the squirrel-cage end ring coincide. The parameters tuning the accelerated transient process are as follows: $\alpha = 1.5$ A/W; $m_0 = 1500$; $\gamma = 1.5$. The accelerated transient process operating points 1 and 3 longs 6.8 and 4.8 electric periods of rotor rotation respectively. Then an ordinary transient process follows ($m = 1$) for 1.2 electric periods of rotor rotation. The last half of electric periods of rotor rotation is used to calculate the motor performance. The time discretization step is 0.01 electric periods of rotor rotation.

V. COMPARISON OF THE IM CHARACTERISTICS BEFORE AND AFTER THE OPTIMIZATION

The comparison of the performance characteristics of the IM before and after optimization is shown in Table 4. Mechanical losses consisting of bearing and windage losses is taken as in [38]. Fig. 6, Fig. 7 show the calculated flux density magnitude of the IM before and after optimization.

Line-to-line voltage amplitude in operation point 1 slightly less than the level of 950 V and becomes exactly equal to 950 V during the optimization. The value for the squirrel cage losses $P'_{sc} = P_2 \cdot s/(1-s)$ calculated through slip and mechanical power P_2 is slightly less than that got with the FEM model, which demonstrates that the additional cage losses caused mainly by parasitic harmonics in the airgap is small enough. It can be explained by sufficient values of the airgap and the unfilled area of the rotor slots. The required power of the inverter that is evaluated as $S_{inv} = (3 \times \sqrt{3} \times V_1 \times I_3)/2$ is reduced approximately by $(1.17 - 1.024)/1.17 = 11\%$.

The average losses over points 1 and 3 are reduced more than by half mainly due to the reduction in the armature DC losses by 2.8 and 3.8 times in points 1 and 3 respectively. A decrease in the airgap and mitigating the rotor teeth saturation in operating point 3 additionally contributes to the armature DC losses reduction. However, a decrease in the airgap contributes to parasitic harmonica, which results in an increase in the core losses and the eddy current losses in the armature winding. The squirrel cage losses are also increased likely because of an increase in the slip in both operating points.

TABLE 2. Parameters fixed during optimization of induction motor.

Parameter	Value
Stack length L, mm	400
Stator stack outer radius R_{out}, mm	334
Number of poles	8
Wedge thickness ε_2, mm	2
Thickness of unfilled stator slot area ε_1, mm	3
Number of turns in the stator slot	7
Number of parallel branches	2
Rotor tooth tip width $(b - b_0)/2$, mm	1
Depth of unfilled rotor slot area h_0, mm	5
Specific conductivity of stator winding wire and rotor squirrel cage, MS/m	45

TABLE 3. Operating points of the traction motors.

Parameter	Initial design	After optimization
Inner stator radius R_{inner}, mm	243	248.8
Stator slot width b_p, mm	9	8.83
Height of winding layer h_s, mm	11	14.6
Air gap, mm	4	3.43
Rotor rod thickness b, mm	9	8.56
Rotor rod height h, mm	20	22.2
Squirrel cage end ring thickness, mm	20	21.6
Slip at point 1, %	1	1.01
Slip at point 2, %	2	2.48

VI. COMPARATIVE ANALYSIS OF OPTIMIZED WOUND ROTOR SYNCHRONOUS MOTOR AND INDUCTION MOTOR CHARACTERISTICS

In this section, a comparison is made between the optimized designs of the WRSM and the IM by analyzing their

TABLE 4. Comparison of performances of the induction motor before and after optimization.

Parameter	Before optimization		After optimization	
Operating point i	1	3	1	3
Rotational speed n, rpm	4000	400	4000	400
Amplitude of the armature phase current I_{arm}, A	223	495	226	416
Efficiency η, %	95.2	84.7	95.2	90.1
Output mechanical power P_2, kW	370	370	370	370
Input active power P_1, kW	389	437	389	411
Armature DC copper loss $P_{arm\ DC}$, kW	11.42	56.35	8.47	28.56
Armature eddy current copper loss $P_{arm\ AC}$, kW	1.37	0.16	2.79	0.15
Stator lamination loss $P_{iron\ st}$, kW	1.59	2.65	2.39	2.39
Rotor lamination loss $P_{iron\ rt}$, kW	0.48	0.07	0.87	0.07
Squirrel cage losses P_{sc}, kW	3.98	7.82	4.05	9.62
Squirrel cage losses through slip P_{sc}', kW	3.74	7.56	3.79	9.42
Total loss P_{loss}, kW	18.84	67.05	18.57	40.79
Average losses over points 1 and 3 $< P_{loss} >$, kW	42.95		29.68	
Power factor	0.77	0.61	0.72	0.75
Line-to-line voltage amplitude V_{arm}, V	909	557	948	508
Torque ripple, %	4.3	1.8	7.0	2.7
Required invertor power S_{inv}, MVA	1.17		1.024	

characteristics. Table 5 presents the performance comparison of the performance of the two machines after optimization.

The optimized characteristics of the IM in Table 5 at operating points 1 and 3 repeat those in Table 4. The characteristics of the optimized IM at operating point 2 are calculated with the slips of 1.3%, 1.4%, and 1.5%. The results with the slips of 1.4% with the lowest total losses are selected for presentation in Table 5. The article [38] contains a detailed description of the design methods and results of the WRSM. In calculating the efficiency of the WRSM, it is assumed that the losses of the wireless exciter account for 10% of the excitation winding losses. Table 6 compares the mass and cost of active materials and the main dimensions of the IM and WRSM.

Torque ripple ΔT, the values of which are shown in Table 5, are calculated using the formula:

$$\Delta T = (T_{max} - T_{min})/T, \tag{14}$$

where T_{max} is the maximum instantaneous torque value; T_{min} is the minimum instantaneous torque value.

Fig. 8 shows the calculated waveforms of the WRSM torque. Fig. 9 shows the calculated waveforms of the IM torque. The lower torque ripple of the IM is due to the greater number q of stator slots per pole and per phase, as well as the greater number of rotor slots.

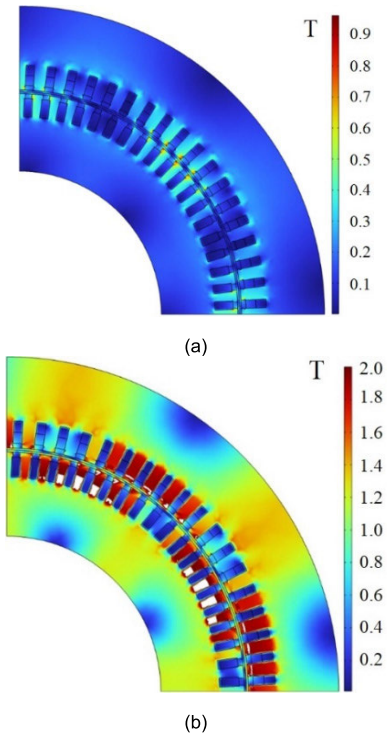

FIGURE 6. Flux density magnitude in the cross section of the optimized IM design at various operating points; areas of white color mark the extreme saturation level (>2 T): (a) operating point 1; (b) operating point 3.

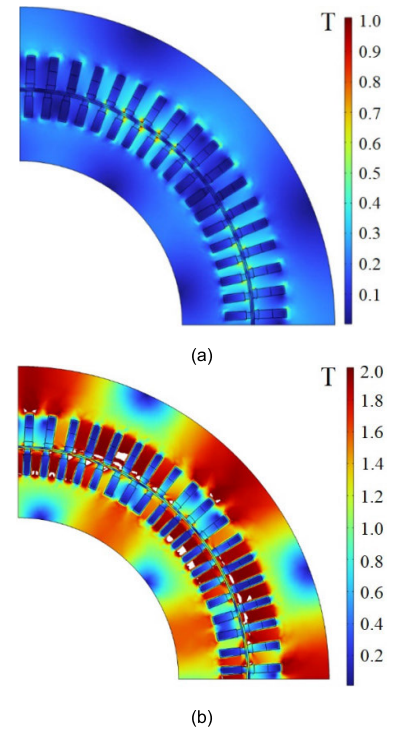

FIGURE 7. Flux density magnitude in the cross section of the optimized IM design at various operating points; areas of white color mark the extreme saturation level (>2 T): (a) operating point 1; (b) operating point 3.

Comparing the characteristics of the IM and WRSM shown in Table 5 and Table 6, the following conclusions can be drawn:

1) Losses for the WRSM, compared to the IM, are by $100\% \cdot (18.6 - 16.9)/18.6 = 9.1\%$ less at operating point 1 at maximum speed; by $100\% \cdot (13.7 - 12.0)/13.7 = 13.7\%$ at operating point 2; by $100\% \cdot (40.84 - 31.1)/40.8 = 23.8\%$ at operating point 3 with maximum torque;

2) The length of the stator of the WRSM without taking into account the armature end parts is less than that of the IM by $100\% \cdot (400 - 330)/400 = 17.5\%$;

3) The mass of active materials of the WRSM is less than that of the IM by $100\% \cdot (817 - 690.5)/817 = 15.5\%$. At the same time, the cost of the WRSM active materials is lower by $100\% \cdot (1807 - 1488)/1807 = 17.7\%$;

4) The mass of active materials of the WRSM rotor is by $100\% \cdot (330 - 279.7)/330 = 15\%$ less than that of the IM. Reducing the mass of the rotor increases the service life of the bearings;

5) The copper mass of the WRSM reduced by $100\%[(539 + 616) - (489 + 442)]/(539 + 616) = 19.4\%$. Reducing the mass of copper for the WRSM is possible, both by reducing the length of the stator lamination, and due to more rational use of copper in the rotor. In the IM, the current in each and the rotor rods is phase-shifted relative to neighboring bars, and the distribution of current in the rods is not the same at each moment of time (Fig. 10a, Fig. 10a). Thus, at each moment of time, some individual rods of the IM rotor turn out to be underloaded by current. Similarly, not all teeth of the IM rotor are uniformly loaded with magnetic flux (Fig. 10b, Fig. 10b). Moreover, additional losses arise in the squirrel cage due to the inhomogeneity of the current distribution over the cross section of the rods and the induction of non-fundamental harmonic currents.

As can be seen from Fig. 10, at operating point 1 at the slot opening near the air gap, the currents are very different from the currents in the rest of the rod, and a strong weakening of the field is visible: loaded rotor teeth are located opposite the loaded slots of the stator winding. Fig. 11 shows that at operating point 3, the currents in the slots of the squirrel cage are quite uniform, and a shift of the squirrel cage currents relative to the stator winding currents is visible.

At the same time, the WRSM uses a single-phase excitation winding. All its conductors are uniformly loaded with excitation current (see Fig. 12a, Fig. 13a), and all rotor teeth are uniformly loaded with magnetic flux (see Fig. 12b, Fig. 13b). The coils of the excitation winding consist of individual small-section conductors rather than from massive rods, which virtually eliminates current inhomogeneity. In the single-phase excitation winding, direct excitation current predominates. Other current harmonics are induced in it to a much lesser extent.

6) An additional factor that increases the cost of the WRSM is the use of a brushless exciter. The exact cost of the brushless exciter is not estimated in this study for the following reasons: 1) The low rated power of the exciter, compared to the inverter supplying the stator winding, means that the cost of the rectifier elements and other exciter semiconductor elements is much less than the cost of the inverter power modules; 2) An accurate estimate of the cost of the rotating transformer of the brushless exciter, to the best of our knowledge, is not presented in the literature. However due to the low rated power of the excitation circuit and the location of the rotating transformer in a small space under the end parts of the armature winding of the WRSM [30], its cost is also significantly less than the cost of the inverter power switch modules;

7) In addition to the amplitude and frequency of the stator current, the load parameter of the IM is the rotor slip. It determines both the amplitude of the squirrel cage current and its field weakening effect. In WRSM, the excitation current and the current angle (the angle between the excitation current and the armature current that determines the field weakening effect) can be controlled independently. This gives great opportunities for choosing the most effective operating conditions in the field weakening region.

TABLE 5. Comparison of the optimized WRSM and IM.

Parameter	WRSM			IM		
Operating point i	1	2	3	1	2	3
Rotational speed n, rpm	4000	1265	400	4000	1265	400
Torque T, N·m	883	2793	8833	883	2793	8833
Amplitude of the armature phase current I_{arm}, A	158	162	292	226	215	416
Efficiency η, % *	95.6	96.9	92.3	95.2	96.4	90.1
Output mechanical power P_2, kW	370	370	370	370	370	370
Input active power P_1, kW	387	382	401	389	384	411
Armature DC copper loss $P_{arm\,DC}$, kW	4.73	4.97	16.10	8.47	7.60	28.56
Armature eddy current copper loss $P_{arm\,AC}$, kW	4.11	0.61	0.22	2.79	0.36	0.15
Stator lamination loss $P_{iron\,st}$, kW	5.11	2.84	2.70	2.39	2.98	2.39
Rotor lamination loss $P_{iron\,rt}$, kW	0.51	0.12	0.04	0.87	0.25	0.07
Excitation copper loss for WRSM P_{exc}, kW	2.41	3.43	12.02	-	-	-
Squirrel cage loss for IM P_{sc}, kW	-	-	-	4.05	2.69	9.62
Total loss P_{loss}, kW **	16.9	12.0	31.1	18.6	13.9	40.8
Power factor	1.00	1.00	0.92	0.72	0.77	0.75
Line-to-line voltage amplitude V_{arm}, V	950	947	603	948	895	508
Torque ripple ΔT, %	11.2	5.2	2.5	7.0	6.5	2.7

Notes: * the IM efficiency is calculated as $\eta = P_2/P_1 = P_2/(P_2 + P_{loss})$, the WRSM efficiency is calculated as $\eta = P_2/(P_1 + P_{exc}) = P_2/(P_2 + P_{loss})$ where P_1 is the active power in armature winding; P_{ex} is the loss in the excitation winding; P_2 is the output (mechanical) power. ** The total loss for IM is calculated as a sum as the following $P_{loss} = P_{arm\,DC} + P_{arm\,AC} + P_{iron\,st} + P_{iron\,rt} + P_{sc}$; the total loss for WRSM is calculated as a sum as the following $P_{loss} = P_{arm\,DC} + P_{arm\,AC} + P_{iron\,st} + P_{iron\,rt} + P_{exc}$. The windage loss and bearing loss are not considered.

VII. INVERTER RATING SELECTION AND POWER MODULE TEMPERATURE RIPPLE ANALYSIS FOR THE IM AND WRSM DRIVES

This section presents the comparative results of the calculation of losses and time plots of temperature in the inverter switches when using the WRSM and IM.

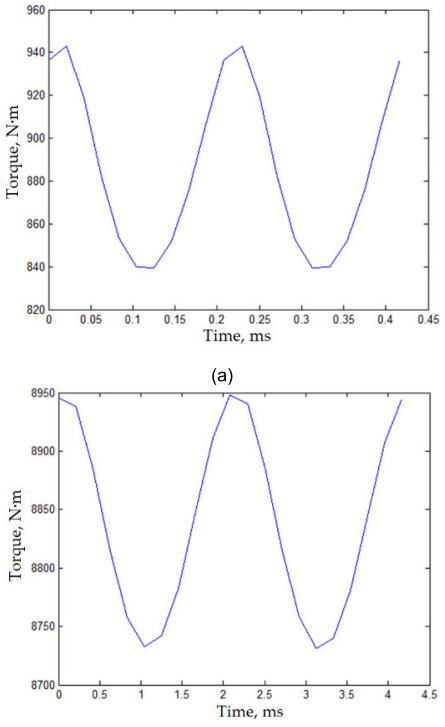

FIGURE 8. WRSM torque waveforms: (a) operating point 1; (b) operating point 3.

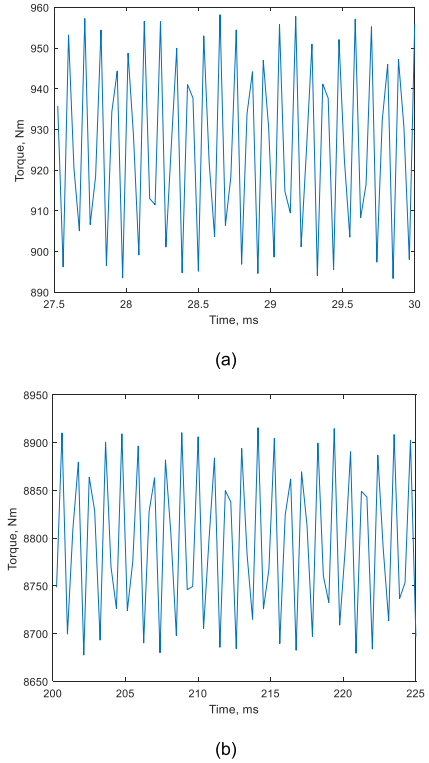

FIGURE 9. IM torque waveforms: (a) operating point 1; (b) operating point 3.

When choosing the inverter power modules for a specific DC-link voltage, the maximum motor current is the primary factor. Moreover, the inverter power module's current rating should be overrated to consider the potential inaccuracies in the theoretical motor characteristics and the mechanical output characteristics in Fig. 4. Another reason for overrating

TABLE 6. Comparison of masses, costs, and some dimensions of the optimized WRSM and IM.

Parameter	WRSM	IM
Stator lamination mass, kg	341	410
Rotor lamination mass, kg	216.6	242
Armature copper mass, kg	69.8	77
Excitation/squirrel cage copper mass, kg	63.1	88
Mass of the rotor active materials, kg	279.7	330
Total mass of active materials, kg	690.5	817
Stator lamination cost, USD	341	410
Rotor lamination cost, USD	217	242
Armature copper cost, USD	489	539
Excitation copper cost, USD	442	616
Total cost of laminations and copper, USD *	1488	1807
Total length of the stator lamination, mm	330	400
Total length of the machine including the winding end parts, mm	579	649
Stator lamination outer diameter, mm	668	668
Air gap, mm	4.17	3.43

Note: the following material costs are assumed: copper—USD 7/kg, steel—USD 1/kg [46].

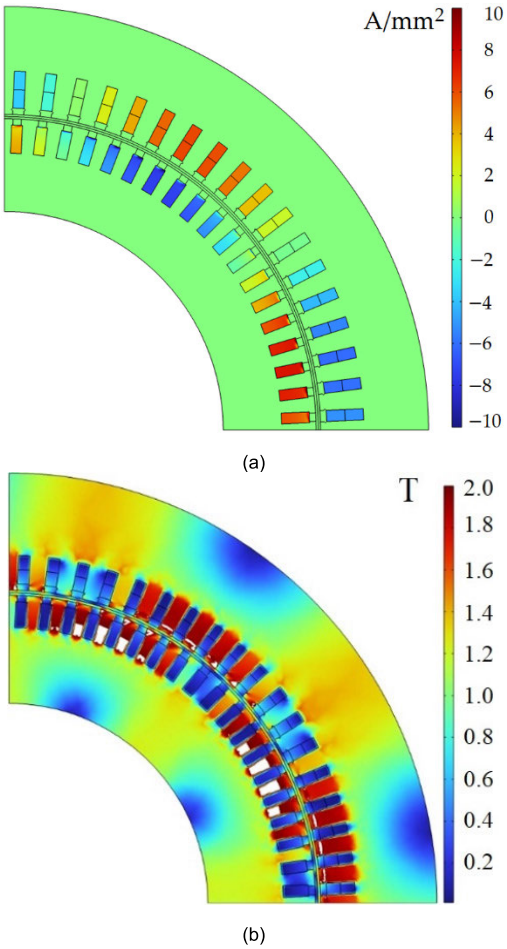

FIGURE 10. Operating point 1 of the IM: (a) Current density; (b) Magnitude of the flux density.

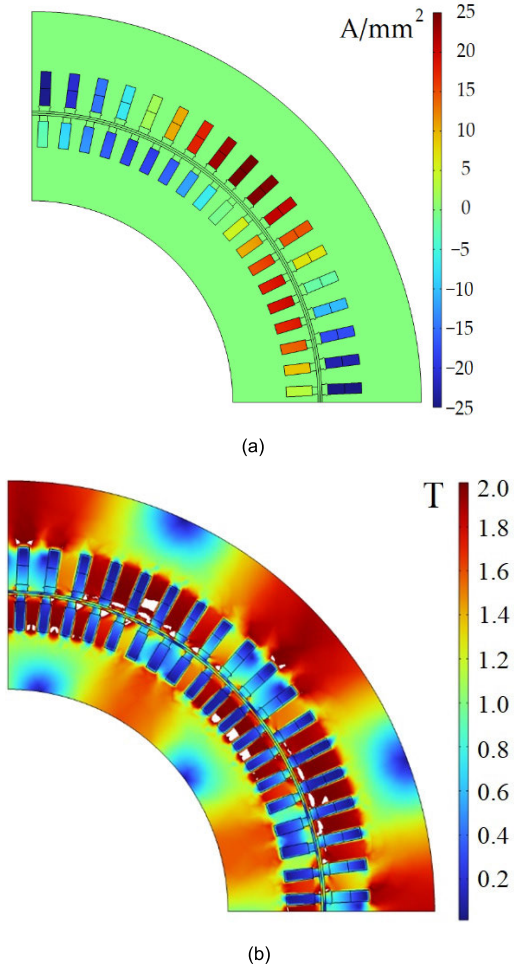

FIGURE 11. Operating point 3 of the IM: (a) Current density; (b) Magnitude of the flux density.

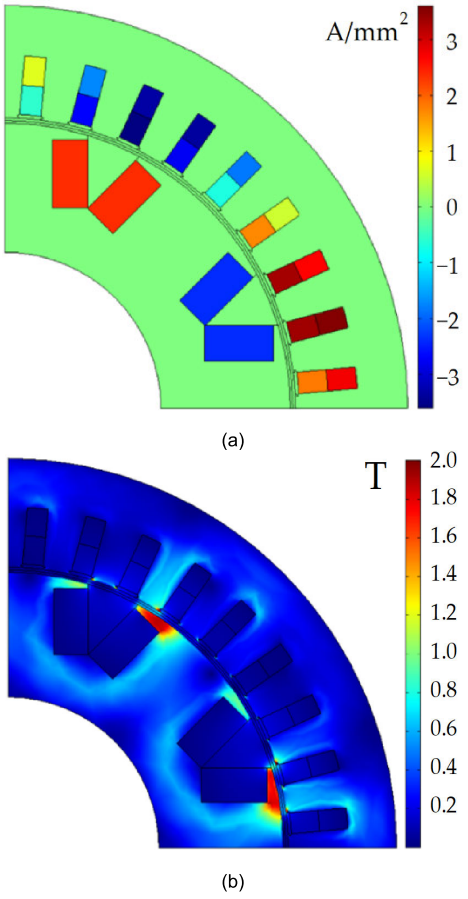

FIGURE 12. Operating point 1 of the WRSM: (a) Current density; (b) Magnitude of the flux density.

the inverter power modules can be large temperature ripple during long-term operation, which shorten the service life of the modules [13], [46]. In particular, for an induction drive of a mining dump truck in the stop mode on a slope with a fully electric brake, long-term, large-amplitude temperature fluctuations occur in the power switches [37]. These ripples are due to the rotor slip frequency current required to generate torque by the induction machine at zero shaft speed.

For these reasons, it is common practice to select a power module for powering a traction IM with double or more current margin, for example, in [47] it is shown that for mining dump truck drives with a maximum current of up to 1500 A, SKiiP-4 power modules with increased stability to thermal cycling with a rated current of 3600 A are selected. As Table 5 shows, the amplitude of the maximum continuous current of the IM is 325 A. Based on the two-fold current margin ($325 \cdot 2 = 650$ A), it is advisable to choose the power module FF650R17IE4 to supply the IM.

The traction inverter for the WRSM does not suffer from temperature ripple during slope stop braking because DC currents flow through the phase windings of the synchronous machine to generate braking torque at zero speed. For this reason, the destructive effect of thermal cycling on the inverter when using the WRSM is significantly reduced, and the margin for rated current may not be so large: for the WRSM with a maximum current of 292 A, as shown in Table 5, it is enough to use the FF450R17IE4 power module. Thus, the WRSM has a significant advantage in the electric brake mode when stopping on a slope. In the IM, due to the presence of the slip, very large temperature ripple occurs, which negatively affects the service life of the inverter switches. In the WRSM, in this mode, DC currents flow through the phases, which helps to avoid the large temperature ripples.

Let us compare the losses, temperature, and temperature ripple of the inverter switches at the operating point with the maximum torque ($i = 3$) for the WRSM and IM. The calculations were made using the IPOSIM software [48] based on the obtained values of the current and voltage of the motors, as well as the characteristics of the power modules. Table 7 shows the comparison of the loss and temperature for the WRSM and IM at maximum torque and speed of 400 rpm.

Fig. 12 illustrates the temperature ripple of the inverter switch elements for this case. The temperature fluctuations of IGBT and freewheel diode have a detrimental effect on their lifespan. The temperature of these components periodically

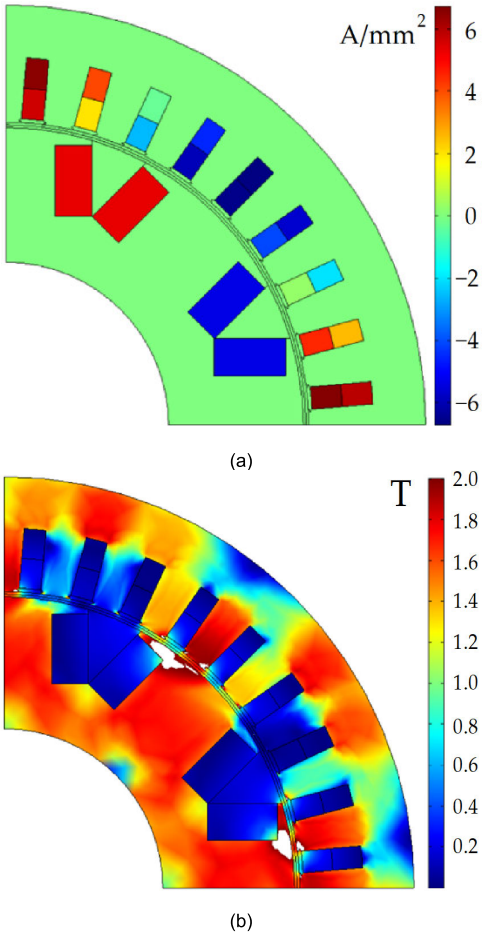

FIGURE 13. Operating point 3 of the WRSM: (a) Current density; (b) Magnitude of the flux density.

changes over time with a large amplitude. At 400 rpm, the freewheel diode's maximum temperature in the WRSM is slightly lower by $96.89 - 94.93 = 2.96$ degrees compared to the IM, while the IGBT's temperature is slightly higher by $101.14 - 100.54 = 0.6$ degrees. The lower loading of the diode in the WRSM is due to a higher power factor.

Table 7 compares inverter loss and temperature for the WRSM and IM at maximum torque and zero speed (electric braking mode during slope stop). Comparison of the results from Table 7 and Table 8 allows us to conclude that the temperature in the switches increases only slightly when using the FF450R17IE4 module, which confirms the possibility of using a less powerful FF450R17IE4 module for the WRSM.

Let us compare the inverter utilization factor $K_i = P_2/S$, which shows the ratio of the mechanical output power of the electric drive and the rated apparent power of the inverter, which is calculated as explained in [38]. For the IM with FF650R17IE4 power module ($V_{DC} = 1000$ V, $I_{C\_nom} = 650$ A) $K_i = 370{,}000/(9 \times 1000 \times 650)/(2 \cdot \sqrt{3}) = 0.219$. For the WRSM with FF450R17IE4 power module ($V_{DC} = 1000$ V, $I_{C\_nom} = 450$ A) $K_i = 370{,}000/(9 \times 1000 \times 450)/(2 \cdot \sqrt{3}) = 0.316$. Thus, the use of the WRSM makes it possible to increase the inverter utilization factor from 0.219 to 0.316. In addition, the inverter for the WRSM is more reliable, since when stopping on a slope, large low-frequency temperature ripple does not occur in the power modules of the WRSM inverter, while the temperature ripple of about 35 °C occurs in the inverter of the IM.

According to [49], the cost of the FF650R17IE4 module is USD 612, while the FF450R17IE4 module is priced at USD 527. Each module includes 2 power switches for one phase and powering a 9-phase motor requires a total of 9 modules. Therefore, the cost of inverter power modules for the IM is

TABLE 7. Inverter losses and temperature ripple evaluation of the WRSM and IM at 400 rpm.

Parameter	WRSM	IM
IGBT module	FF450R17IE4	FF650R17IE4
PWM frequency f_{PWM}, Hz	2000	
DC link voltage V_{DC}, V	950	
Heatsink temperature, °C	80	
Fundamental frequency f, Hz*	26.6	27.3
RMS phase current, A	206.5	294.2
Line-to-line fundamental voltage amplitude V_a, V	603	508
Modulation index $k_m = V_a/V_{DC}$	0.635	0.535
Power factor	0.92	0.75
Switching loss (IGBT), W	136.33	193.75
Switching loss (reverse diode), W	55.45	68.83
Conduction loss (IGBT), W	112.38	143.38
Conduction loss (reverse diode), W	35.75	63.94
Total loss (IGBT), W	248.71	337.12
Total loss (reverse diode), W	91.20	132.77
Maximum/minimum temperature (IGBT), °C	101.14/93.25	100.54/93.58
Maximum/minimum temperature (reverse diode), °C	94.93/88.23	96.89/89.73
Temperature ripple (IGBT), °C	7.9	7.0
Temperature ripple (reverse diode), °C	6.7	7.2

Note: Fundamental supply frequency $f = (n \times p) / 60 + f_s$, where p is the motor pole number; n is the rotational speed, rpm; f_s is the slip frequency

TABLE 8. Inverter losses and temperature ripple evaluation of The WRSM and IM at zero speed. (Full Electric Brake Mode.)

Parameter	WRSM	IM
IGBT module	FF450R17IE4	FF650R17IE4
PWM frequency f_{PWM}, Hz	2000	
DC link voltage V_{DC}, V	950	
Heatsink temperature, °C	80	
Fundamental frequency $f = (n \times p)/60$, Hz	0	0.7
RMS phase current, A	206.5	294.2
Modulation index $k_m = V_a/V_{DC}$	0.022	0.038
Power factor	1	0.97
Switching loss (IGBT), W	80	80
Switching loss (reverse diode), W	146.02	203.28
Conduction loss (IGBT), W	63.6	79.02
Conduction loss (reverse diode), W	78.99	112.47
Total loss (IGBT), W	67.04	93.82
Total loss (reverse diode), W	225.01	315.75
Temperature ripple (IGBT), °C	0*	36.3
Temperature ripple (reverse diode), °C	0*	39.3

Note: *at zero speed, the temperature ripple when powering the WRSM is zero, since DC currents flow through the phase windings. In the case of the IM, the temperature ripple is not equal to zero, since the slip frequency current flows through the phase windings.

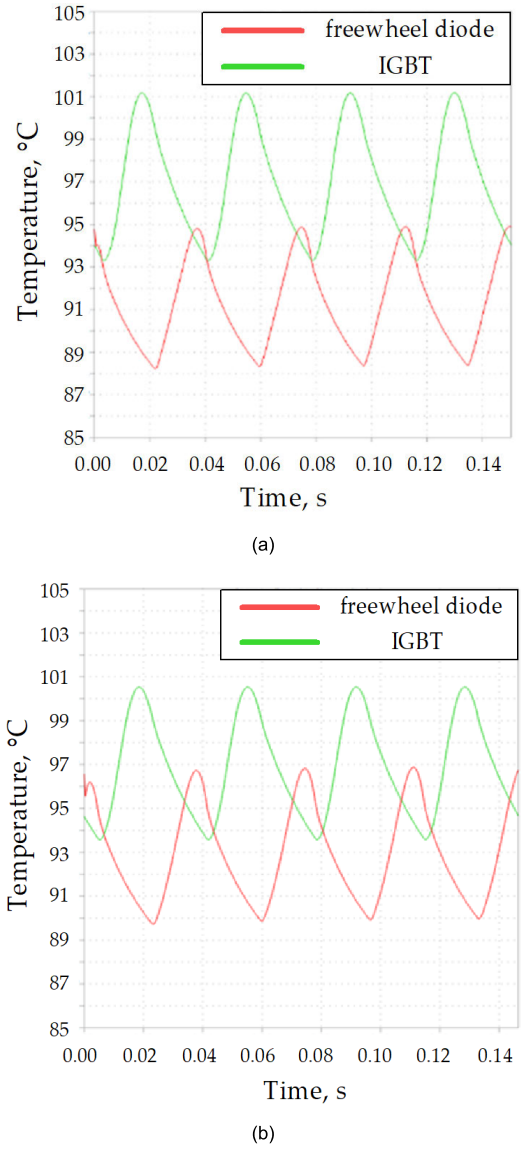

FIGURE 14. Temperature variation of inverter elements (IGBT transistor line shown in red and freewheel diode line shown in green) over time when feeding various motors. (a) WRSM at 400 rpm employing FF450R17IE4 modules; (b) IM at 400 rpm employing FF650R17IE4 modules.

$9 \cdot 585 =$ USD 5508. The cost of inverter power modules for the WRSM is $9 \cdot 527 =$ USD 4743. It can be concluded that the use of the WRSM, in comparison with the IM, allows to reduce the cost of power modules by $5508/4743 = 1.16$ times.

VIII. CONCLUSION

The paper provides a theoretical comparison of various characteristics of the wound rotor synchronous motor (WRSM) and the induction motor (IM) in a mining dump truck drive. Because this application requires the drive to have a wide constant power speed control range (CPSR) of 10:1, optimization and performance analysis of the motors are carried out at various operating points, including in the field weakening region.

The calculated characteristics of the IM are compared with the WRSM characteristics calculated in our previous study [38]. The performance optimization of both the IM and the WRSM at various operating points was carried out using the computationally efficient Nelder-Mead method. The optimization process focused on minimizing power loss in the driving cycle and the power rating of the semiconductor inverter that feeds the motor. Additionally, torque ripple is included in the objective function to limit its value during the optimization process. The calculated characteristics of the IM were then compared to those of the WRSM obtained in a previous study. Both motor designs were optimized using a similar optimization procedure.

The results of a comparative analysis of optimized designs show that the advantage of the IM over the WRSM is the absence of a brushless exciter, which introduces additional cost and reduces reliability. The advantages of the WRSM are the reduction of power loss, length, weight, and cost of active materials. Power loss for the WRSM, compared to IM, is less by 9.1% at operating point 1 at maximum speed; by 13.7% at duty point 2 at medium speed; by 23.8% at duty point 3 with maximum torque. The stator lamination length of the WRSM is less than that of the IM 17.5%. The mass of active materials in the WRSM is less than in the IM by 15.5%. At the same time, the cost of the WRSM active materials is lower by 17.7%. The mass of active materials of the WRSM rotor is 15% less than that of the IM, which increases the service life of the bearings. In addition, the mass of more expensive copper in the WRSM is reduced by 19.4% compared to the IM.

Furthermore, the WRSM allows for a reduction in the cost of inverter power modules by 1.16 times and an increase in the inverter utilization factor from 0.219 to 0.316. This motor also enhances the reliability and service life of the inverter by eliminating power switch temperature ripples in the power modules caused by stopping on slopes with an electric brake which is common in the considered application.

Based on the results of our comparative study, it can be concluded that the use of the WRSM is promising in mining dump trucks, in terms of increased performance and lower cost and mass of active materials, as well as lower cost and higher reliability of inverter power modules. In future works, it is planned to consider in more detail the characteristics of the brushless exciter when using the WRSM in the application under consideration.

REFERENCES

[1] W. G. Koellner, G. M. Brown, J. Rodriguez, J. Pontt, P. Cortes, and H. Miranda, "Recent advances in mining haul trucks," *IEEE Trans. Ind. Electron.*, vol. 51, no. 2, pp. 321–329, Apr. 2004, doi: 10.1109/TIE.2004.825263.

[2] A. F. Abouzeid, J. M. Guerrero, A. Endemaño, I. Muniategui, D. Ortega, I. Larrazabal, and F. Briz, "Control strategies for induction motors in railway traction applications," *Energies*, vol. 13, no. 3, p. 700, Feb. 2020, doi: 10.3390/en13030700.

[3] J. Bernatt, S. Gawron, T. Glinka, and A. Polak, "Traction induction motor," in *Proc. 13th Int. Mod. Electrified Transp. (MET)*, Warsaw, Poland, Oct. 2017, pp. 1–5, doi: 10.1051/matecconf/201818004005.

[4] B. Kim, J. Lee, Y. Jeong, B. Kang, K. Kim, Y. Kim, and Y. Park, "Development of 50 kW traction induction motor for electric vehicle (EV)," in *Proc. IEEE Vehicle Power Propuls. Conf.*, Seoul, South Korea, Oct. 2012, pp. 142–147, doi: 10.1109/VPPC.2012.6422627.

[5] J. Doerr, G. Fröhlich, A. Stroh, and M. Baur, 'The electric drivetrain with three-motor layout of the audi E-tron S," *MTZ Worldwide*, vol. 81, nos. 7–8, pp. 16–25, Jun. 2020, doi: 10.1007/s38313-020-0254-2.

[6] M. Popescu, J. Goss, D. A. Staton, D. Hawkins, Y. C. Chong, and A. Boglietti, "Electrical vehicles—Practical solutions for power traction motor systems," *IEEE Trans. Ind. Appl.*, vol. 54, no. 3, pp. 2751–2762, May 2018, doi: 10.1109/TIA.2018.2792459.

[7] K. Matsuoka and M. Kondo, "Energy saving technologies for railway traction motors," *IEEJ Trans. Electr. Electron. Eng.*, vol. 5, no. 3, pp. 278–284, May 2010, doi: 10.1002/tee.20530.

[8] A. T. de Almeida, F. J. T. E. Ferreira, and G. Baoming, "Beyond induction motors—Technology trends to move up efficiency," *IEEE Trans. Ind. Appl.*, vol. 50, no. 3, pp. 2103–2114, May 2014, doi: 10.1109/TIA.2013.2288425.

[9] L. Fedoseyev and E. M. Pearce Jr., "Rotor assembly with heat pipe cooling system," U.S. Patent 9 331 552 B2, Jun. 13, 2013. [Online]. Available: https://patents.google.com/patent/US20140368064A1/en

[10] Z. Q. Zhu, W. Q. Chu, and Y. Guan, "Quantitative comparison of electromagnetic performance of electrical machines for HEVs/EVs," *CES Trans. Electr. Mach. Syst.*, vol. 1, no. 1, pp. 37–47, Mar. 2017, doi: 10.23919/TEMS.2017.7911107.

[11] A. Vinogradov, V. Chistoserdov, and A. Korotkov, "Algorithms of anti-slip and anti-skid in electric transmissions of mining dump trucks," (in Russian), in *Proc. Int. Sci. Tech. Conf. Status Prospects Develop. Elect. Thermal Technol.*, Russia, Ivanovo, May 2019, pp. 39–42.

[12] S. Hiti, D. Tang, C. Stancu, and E. Ostrom, "Zero vector modulation method for voltage source inverter operating near zero output frequency," in *Proc. IEEE Ind. Appl. Conf., 39th IAS Annu. Meeting*, Seattle, WA, USA, Oct. 2004, pp. 171–176, doi: 10.1109/IAS.2004.1348404.

[13] B. Cougo, L. Morais, G. Segond, R. Riva, and H. T. Duc, "Influence of PWM methods on semiconductor losses and thermal cycling of 15-kVA three-phase SiC inverter for aircraft applications," *Electronics*, vol. 9, no. 4, p. 620, Apr. 2020, doi: 10.3390/electronics9040620.

[14] Y. Ali, E. Kulik, A. Anuchin, and D. H. Do, "Thermal cycling effect in a traction inverter for star-connected and open-end winding permanent magnet synchronous motors with nearly constant losses current regulation," in *Proc. 29th Int. Workshop Electr. Drives, Adv. Power Electron. Electric Drives (IWED)*, Moscow, Russia, Jan. 2022, pp. 1–6, doi: 10.1109/IWED54598.2022.9722583.

[15] MH Sub I LLC, AudiWorld. (Oct. 2020). *How to Finesse and Etron on an Incline and Parallel Parking?* [Online]. Available: https://www.audiworld.com/forums/audi-e-tron-q8-e-tron-232/how-finesse-etron-incline-parallel-parking-3018036/

[16] (Jun. 2022). *Tesla Motor Designer Explains Model 3'S Transition to Permanent Magnet Motor*. [Online]. Available: https://electrek.co/2018/02/27/tesla-model-3-motor-designer-permanent-magnet-motor/

[17] Automotive Powertrain Technology International. (Jul. 2020). *Audi Equips Q4 Sportback e-Tron With PM and Induction Motors*. [Online]. Available: https://www.automotivepowertraintechnologyinternational.com/news/new-engine/audi-equips-q4-sportback-e-tron-with-PM-and-induction-motors.html

[18] A. Dianov, "Instant closing of permanent magnet synchronous motor control systems at open-loop start," *Sustainability*, vol. 14, no. 19, p. 12665, Oct. 2022, doi: 10.3390/su141912665.

[19] R. Schulze, "Reducing environmental impacts of the global rare earth production for use in Nd-Fe-B magnets, how magnetic technologies much can recycling contribute?" Ph.D. dissertation, Dept. Civil Environ. Eng., Darmstadt Tech. Univ., Darmstadt, Germany, Dec. 2018.

[20] S. Dong, W. Li, H. Chen, and R. Han, "The status of Chinese permanent magnet industry and R&D activities," *AIP Adv.*, vol. 7, May 2017, Art. no. 056237, doi: 10.1063/1.4978699.

[21] V. Dmitrievskii, V. Prakht, and V. Kazakbaev, "Synchronous reluctance generator with ferrite magnets for wind turbine," *J. Phys., Conf. Ser.*, vol. 1102, Nov. 2018, Art. no. 012041, doi: 10.1088/1742-6596/1102/1/012041.

[22] I. B. De Lima and W. L. Filho, *Rare Earths Industry: Technological, Economic, and Environmental Implications*. Amsterdam, The Netherlands: Elsevier, 2015.

[23] V. Dmitrievskii, V. Prakht, V. Kazakbaev, and A. Anuchin, "Comparison of interior permanent magnet and synchronous homopolar motors for a mining dump truck traction drive operated in wide constant power speed range," *Mathematics*, vol. 10, no. 9, p. 1581, May 2022, doi: 10.3390/math10091581.

[24] PressClub Global, BMW Group, Press Kit. (Jul. 2020). *The First-Ever BMW iX3*. [Online]. Available: https://www.press.bmwgroup.com/global/article/detail/T0310696EN/the-first-ever-bmw-ix3?language=en and https://www.netcarshow.com/bmw/2021-ix

[25] S. Feustel, B. Huebner, D. Loos, J. Merwerth, Y. Tremaudant, and K. Vollmer, "Rotor for separately excited inner rotor synchronous machine, inner rotor synchronous machine, motor vehicle and method," U.S. Patent 2021 0 006 105 A1, Jul. 15, 2019. [Online]. Available: https://patents.google.com/patent/US20210006105A1

[26] M. R. Raia, M. Ruba, C. Martis, C. Husar, and G. M. Sirbu, "Battery electric vehicle (BEV) powertrain modelling and testing for real-time control prototyping platform integration," in *Proc. 23rd Eur. Conf. Power Electron. Appl. (EPE ECCE Europe)*, Ghent, Belgium, Sep. 2021, pp. P.1–P.10, doi: 10.23919/EPE21ECCEEurope50061.2021.9570616.

[27] *Renault Fluence Z. E. is a Positive Influence*, Torque, Singapore, May 2012. [Online]. Available: https://www.torque.com.sg/reviews/renault-fluence-z-e-is-a-positive-influence/

[28] Renault Group. (Jul. 2022). *All-New Megane e-Tech Electric: Delving Into the Heart of Innovation. Episode 3—A Patent for an Eco-Friendlier Electric Motor*. [Online]. Available: https://www.renaultgroup.com/en/news-on-air/news/all-new-megane-e-tech-electric-delving-into-the-heart-of-innovation-episode-3/

[29] W. Q. Chu, Z. Q. Zhu, J. Zhang, X. Ge, X. Liu, D. Stone, and M. Foster, "Comparison of electrically excited and interior permanent magnet machines for hybrid electric vehicle application," in *Proc. 17th Int. Conf. Electr. Mach. Syst. (ICEMS)*, Hangzhou, China, Oct. 2014, pp. 401–407, doi: 10.1109/ICEMS.2014.7013504.

[30] E. Illiano, "Design of a highly efficient brushless current excited synchronous motor for automotive purposes," Ph.D. dissertation, ETH-Zürich, Zürich, Switzerland, 2014, doi: 10.3929/ethz-a-010433793.

[31] J. K. Nøland, S. Nuzzo, A. Tessarolo, and E. F. Alves, "Excitation system technologies for wound-field synchronous machines: Survey of solutions and evolving trends," *IEEE Access*, vol. 7, pp. 109699–109718, 2019, doi: 10.1109/ACCESS.2019.2933493.

[32] M. Maier and N. Parspour, "Operation of an electrical excited synchronous machine by contactless energy transfer to the rotor," *IEEE Trans. Ind. Appl.*, vol. 54, no. 4, pp. 3217–3225, Jul. 2018, doi: 10.1109/TIA.2018.2814558.

[33] I. Boldea, G. D. Andreescu, C. Rossi, A. Pilati, and D. Casadei, "Active flux based motion-sensorless vector control of DC-excited synchronous machines," in *Proc. IEEE Energy Convers. Congr. Expo.*, San Jose, CA, USA, Sep. 2009, pp. 2496–2503, doi: 10.1109/ECCE.2009.5316509.

[34] C. Stancu, T. Ward, K. Rahman, R. Dawsey, and P. Savagian, "Separately excited synchronous motor with rotary transformer for hybrid vehicle application," in *Proc. IEEE Energy Convers. Congr. Expo. (ECCE)*, Pittsburgh, PA, USA, Sep. 2014, pp. 5844–5851, doi: 10.1109/ECCE.2014.6954203.

[35] *MAHLE Develops Highly Efficient Magnet-Free Electric Motor*, MAHLE Group, Stuttgart, Germany, May 2021. [Online]. Available: https://www.mahle.com/en/news-and-press/press-releases/mahle-develops-highly-efficient-magnet-free-electric-motor–82368.

[36] *Mahle's Cheap, Highly Efficient New EV Motor Uses no Magnets*, MAHLE Group, Stuttgart, Germany, May 2021. [Online]. Available: https://newatlas.com/automotive/mahle-magnet-free-electric-traction-motor/

[37] S. Mirzaei and A. Fernandez, "Retard system solution on electric mining trucks," in *Proc. 3rd IEEE Int. Symp. Sensorless Control Electr. Drives (SLED)*, Milwaukee, WI, USA, Sep. 2012, pp. 1–5, doi: 10.1109/SLED.2012.6422816.

[38] V. Prakht, V. Dmitrievskii, V. Kazakbaev, and A. Anuchin, "Comparative study of electrically excited conventional and homopolar synchronous motors for the traction drive of a mining dump truck operating in a wide speed range in field-weakening region," *Mathematics*, vol. 10, no. 18, p. 3364, Sep. 2022, doi: 10.3390/math10183364.

[39] G. Pellegrino, A. Vagati, B. Boazzo, and P. Guglielmi, "Comparison of induction and PM synchronous motor drives for EV application including design examples," *IEEE Trans. Ind. Appl.*, vol. 48, no. 6, pp. 2322–2332, Nov. 2012, doi: 10.1109/TIA.2012.2227092.

[40] K. Aiso and K. Akatsu, "Performance comparison of high-speed motors for electric vehicle," *World Electric Vehicle J.*, vol. 13, no. 4, p. 57, Mar. 2022, doi: 10.3390/wevj13040057.
[41] A. Anuchin, D. Aliamkin, M. Lashkevich, D. Shpak, A. Zharkov, and F. Briz, "Minimization and redistribution of switching losses using predictive PWM strategy in a voltage source inverter," in *Proc. 25th Int. Workshop Electric Drives: Optim. Control Electric Drives (IWED)*, Moscow, Russia, Jan./Feb. 2018, pp. 1–6, doi: 10.1109/IWED.2018.8321375.
[42] N. Bianchi, *Electrical Machine Analysis Using Finite Elements*. Boca Raton, FL, USA: CRC Press, 2005, doi: 10.1201/9781315219295.
[43] A. Selema, M. Gulec, M. N. Ibrahim, R. Sprangers, and P. Sergeant, "Selection of magnet wire topologies with reduced AC losses for the windings of electric drivetrains," *IEEE Access*, vol. 10, pp. 121531–121546, 2022, doi: 10.1109/ACCESS.2022.3222773.
[44] S. Guo, H. Zhao, Y. Wang, X. Yin, H. Qi, P. Li, and Z. Lin, "A design technique of traction motor for efficiency improvement based on multiobjective optimization," *World Electr. Vehicle J.*, vol. 12, no. 4, p. 260, Dec. 2021, doi: 10.3390/wevj12040260.
[45] Y. Sun, Y. Fang, Q. Zhang, and Q. Liu, "Optimal design of marine motors for joint efficiency and economic optimization," *Energies*, vol. 16, no. 12, p. 4588, Jun. 2023, doi: 10.3390/en16124588.
[46] J. Goss, M. Popescu, and D. Staton, "A comparison of an interior permanent magnet and copper rotor induction motor in a hybrid electric vehicle application," in *Proc. Int. Electr. Mach. Drives Conf.*, Chicago, IL, USA, May 2013, pp. 220–225, doi: 10.1109/IEMDC.2013.6556256.
[47] JSC NIPTIEM. (Jan. 2017). *Sets of Traction Electrical Equipment for Heavy-Duty Mining Dump Trucks*, (in Russian). [Online]. Available: http://vectorgroup.ru/articles/DP_2017_1
[48] Infineon Technologies. *Infineon Online Power Simulation Platform*. Accessed: Jul. 7, 2023. [Online]. Available: https://www.infineon.com/cms/en/tools/landing/iposim-infineon-online-power-simulation-platform
[49] Infineon Technologies. *IGBT Modules, Infineon Online Catalogue*. Accessed: Jul. 7, 2023. [Online]. Available: https://www.infineon.com/cms/en/product/power/igbt/igbt-modules

VLADIMIR DMITRIEVSKII received the master's degree in theoretical physics and the Ph.D. degree from Ural Federal University, Yekaterinburg, Russia, in 1996 and 2007, respectively. He submitted his Ph.D. dissertation on mathematical modeling and optimal designing the linear electric motors, in 2006. He is currently an Associate Professor with the Department of Electrical Engineering, Ural Federal University. His research interests include optimal designing energy-efficient motors and developing sensorless control algorithms for electric drives.

VLADIMIR PRAKHT received the M.Eng. degree in engineering and the Ph.D. degree from the Department of Electrical Engineering, Ural Federal University, Yekaterinburg, Russia, in 2004 and 2007, respectively. He submitted his Ph.D. dissertation on optimal control and mathematical modeling induction heating systems, in 2006. He is currently an Associate Professor with the Department of Electrical Engineering, Ural Federal University. His research interests include mathematical modeling and optimal design of energy efficient electric motors and generators.

EDUARD VALEEV is currently pursuing the master's degree with the Department of Electrical Engineering, Ural Federal University. He is a Laboratory Assistant with the Department of Electrical Engineering, Ural Federal University. His research interest includes modeling of electrical drive systems.

ALEKSEY PARAMONOV is currently pursuing the master's degree with the Department of Electrical Engineering, Ural Federal University. He is a Laboratory Assistant with the Department of Electrical Engineering, Ural Federal University. He prepared and published several articles on electrical system modeling in scientific peer-reviewed journals. His research interests include modeling of electrical machines and electrical drive systems.

VADIM KAZAKBAEV received the M.Eng. degree in engineering and the Ph.D. degree from the Department of Electrical Machines, Ural Federal University, Yekaterinburg, Russia, in 2010 and 2017, respectively. He submitted his Ph.D. dissertation on "Development of High-Performance Synchronous Reluctance Motor", in 2016. He is currently a Junior Researcher and an Associate Professor with the Department of Electrical Engineering, Ural Federal University. His research interests include electrical engineering, design of electrical machines, and control of electrical drives.

ALECKSEY ANUCHIN (Senior Member, IEEE) received the B.Sc., M.Sc., Ph.D., and Dr.Eng.Sc. degrees from Moscow Power Engineering Institute, Moscow, Russia, in 1999, 2001, 2004, and 2018, respectively. He delivers lectures on "control systems of electric drives," "real-time software design," "electric drives," and "science research writing" with Moscow Power Engineering Institute. He has been the Head of the Electric Drives Department, for the last eight years. He has more than 20 years of experience covering control systems of electric drives, hybrid powertrains, and real-time communications. He is the author of three textbooks on the design of real-time software for the microcontroller of the C28 family and Cortex-M4F, and control system of electric drives, in Russian. He has authored or coauthored more than 100 conference and journal papers.